Naval Research Laboratory

Washington, DC 20375-5000

NRL Memorandum Report 6412

Simulations of Axisymmetric Erosion in IFR-Transported Beams

J. KRALL*, K. NGUYEN** AND G. JOYCE

*Science Applications Int. Corp., McLean, VA

**Naval Surface Warfare Center, Silver Spring, MD

Plasma Theory Branch
Plasma Physics Division

February 21, 1989

SECURITY CLASSIFICATION OF THIS PAGE

REPORT DOCUMENTATION PAGE

1a REPORT SECURITY CLASSIFICATION UNCLASSIFIED	1b RESTRICTIVE MARKINGS
2a SECURITY CLASSIFICATION AUTHORITY	3 DISTRIBUTION AVAILABILITY OF REPORT Approved for public release; distribution unlimited.
2b DECLASSIFICATION / DOWNGRADING SCHEDULE	
4 PERFORMING ORGANIZATION REPORT NUMBER(S) NRL Memorandum Report 6412	5 MONITORING ORGANIZATION REPORT NUMBER(S)
6a NAME OF PERFORMING ORGANIZATION Naval Research Laboratory 6b OFFICE SYMBOL (If applicable) Code 4790	7a NAME OF MONITORING ORGANIZATION Naval Surface Warfare Center
6c ADDRESS (City, State, and ZIP Code) Washington, DC 20375-5000	7b ADDRESS (City, State, and ZIP Code) Silver Spring, MD 20903-5000
8a NAME OF FUNDING/SPONSORING ORGANIZATION DARPA 8b OFFICE SYMBOL (If applicable)	9 PROCUREMENT INSTRUMENT IDENTIFICATION NUMBER JO #47-0900-0-9
8c ADDRESS (City, State, and ZIP Code) Arlington, VA 22209	10 SOURCE OF FUNDING NUMBERS PROGRAM ELEMENT NO: 62707E PROJECT NO: ARPA Order 4795 A69 TASK NO: WORK UNIT ACCESSION NO: AN180-127

11 TITLE (Include Security Classification)

Simulations of Axisymmetric Erosion in IFR-Transported Beams

12 PERSONAL AUTHOR(S)
Jonathan Krall,* Khanh Nguyen,** and Glenn Joyce

13a TYPE OF REPORT	13b TIME COVERED	14 DATE OF REPORT (Year, Month, Day)	15 PAGE COUNT
Interim	FROM _____ TO _____	1989 February 21	39

16 SUPPLEMENTARY NOTATION
* Science Applications Intl. Corp., McLean, VA
**Naval Surface Warfare Center, Silver Spring, MD

17 COSATI CODES		
FIELD	GROUP	SUB-GROUP

18 SUBJECT TERMS (Continue on reverse if necessary and identify by block number)
Relativistic electron beam; Particle simulation code; [illegible]lation code; Hose instability; Beam propagation code; [illegible]tion code; IFR transport

19 ABSTRACT (Continue on reverse if necessary and identify by block number)

Erosion rates for a relativistic electron beam propagating through a low density plasma channel in the ion-focused regime are computed via axisymmetric particle simulation. We find steady-state inductive (ohmic) erosion rates that are in quantitative agreement with new theoretical results which correctly account for the relativistic dynamics of electrons at the beam head. In cases where the finite emittance of the beam is expected to be the dominant loss mechanism, the beam does not develop steady-state erosion, as suggested by previous analyses. Asymptotically, such a beam is characterized by a low emittance population at the beam head, a long rise length, and an erosion rate that tends toward zero.

20 DISTRIBUTION/AVAILABILITY OF ABSTRACT	21 ABSTRACT SECURITY CLASSIFICATION
☐ UNCLASSIFIED/UNLIMITED ☒ SAME AS RPT ☐ DTIC USERS	UNCLASSIFIED
22a NAME OF RESPONSIBLE INDIVIDUAL Glenn Joyce	22b TELEPHONE (Include Area Code) (202) 767-6785 22c OFFICE SYMBOL Code 4790

DD FORM 1473, 84 MAR 83 APR edition may be used until exhausted
All other editions are obsolete

SECURITY CLASSIFICATION OF THIS PAGE

CONTENTS

SIMULATIONS OF AXISYMMETRIC EROSION IN IFR-TRANSPORTED BEAMS

I. Introduction

An electron beam propagating along a low density plasma channel in the ion focused regime (IFR) is characterized by a freely expanding head, a pinch region, where the plasma electrons are ejected from the channel and the beam pinches to its equilibrium value, and the beam body. When $N_c < N_b$, where N_c is the line density of the plasma channel electrons and N_b is the line density of the beam electrons, the channel electrons are fully expelled from the vicinity of the beam and the remaining ions reduce its space charge potential. This has allowed stable propagation of intense beams over distances of several tens of meters, as demonstrated, for example, in the Advanced Test Accelerator.[1] The pinch region of the beam is associated with increasing net current and azimuthal magnetic field and an inductive E_z spike. Energy loss, due to the inductive field, causes electrons to be removed from the beam head. Additional particle losses can result from the finite emittance of the portion of the beam that is not fully pinched. Both of these processes cause the pinch point to erode backwards in the beam frame. These beams are also subject to instabilities, such as the transverse two-stream and ion hose instabilities.[2,3,4] In the present paper, we work within the constraint of azimuthal symmetry, in which the dominant (transverse) instabilities are not present.

The physics of IFR propagation has developed over a number of years and was recently discussed in some detail.[2,5] We will focus on the transport losses associated with inductive and emittance effects at the beam head. To complement and illuminate the previous analyses, we perform particle simulations in sufficient detail that erosion rates can be measured directly from the motion of the pinch point relative to the motion of the beam body. Such simulations have not been previously presented.

Manuscript approved December 21, 1988

The simulations are a product of FRIEZR, a fully electromagnetic two-dimensional (r,z) particle code that has recently been developed to study IFR propagation and transport of electron beams. It features fully relativistic beam and channel electrons and treats the ions as an immobile fluid. A notable feature of the code is that it solves Maxwell's equations and propagates the beam in a coordinate system which moves at the speed of light. The coordinates are r,ζ,τ where $\zeta = ct - z$ and $\tau = t$. An eroding beam appears to move slowly backwards in these coordinates. FRIEZR is discussed in the appendix.

The remainder of this paper proceeds as follows. In section II we derive a new expression for steady-state inductive erosion which is valid in cases where scattering and secondary ionization may be neglected. Simulation results are then presented for comparison. In section III, we cite previous analyses of emittance-driven erosion and compare these results with simulations. Here, we will find that the assumption of self-similar radial expansion of the beam head that is contained in these analyses does not hold. The simulations provide some insights into the relevant physics. Section IV concludes.

II. Inductive Erosion

In IFR propagation, where energy losses due to scattering may be neglected, the inductive (ohmic) erosion rate per unit propagation distance of a beam pulse may be simply approximated by

$$\frac{\beta_o - \beta_p}{\beta_p} = \frac{\Delta\zeta}{\Delta z} \simeq \frac{\zeta_{max}}{\text{range}} , \qquad (1)$$

where ζ_{max} is the pulse length, β_o is the beam velocity normalized to c and β_p is the velocity of the pinch point so that $\beta_o - \beta_p$ is the rate of beam

loss with respect to time. Note that the first equality above implies that losses are confined to the beam head, as is the case when scattering and radiation losses may be neglected. This also requires that the beam be matched to the plasma channel, so that the beam body is in equilibrium.

The range, which appears in Eq. (1) above, may be calculated from the beam energy that is lost to the inductive axial electric field per unit propagation distance and the available energy of the beam electrons. Using a reduced set of Maxwell's equations for relativistic beams, the electric field at a fixed radius $r = r_c$ has been calculated to be[2]

$$E_z(r_c,\zeta) = \frac{2}{c} \log\left(\frac{r_w}{r_c}\right) \frac{\partial}{\partial\zeta}(fI_b) \ , \qquad (2)$$

where r_c is the radius of the plasma channel, $f = N_c/N_b$ is the ratio of the line densities of channel ions to beam electrons and I_b is the beam current (taken to be positive), rises from zero at $\zeta = 0$ to reach a constant value behind the pinch point. In deriving (2) it was assumed that the plasma electrons are ejected from the channel and move out to a conducting boundary at a finite radius r_w. Beam energy lost to the induced field is transferred to the channel electrons as they are moved to large radii and the channel potential is established. The assumption of a finite conducting boundary is necessary because of the logarithmic nature of this potential. Averaged over the entire pulse (2) gives

$$\bar{E}_z = \frac{1}{\zeta_{max}} \int_0^{\zeta_{max}} E_z(r_c,\zeta)\, d\zeta$$

$$= \frac{L_c f I_b}{c\zeta_{max}} \Big|_{\zeta=\zeta_{max}} \ , \qquad (3)$$

where $L_c = 2\log(r_w/r_c)$ is a dimensionless inductance. The range may now be calculated as

$$\text{range} = \frac{(\gamma_{inj} - \gamma_f)mc^2}{e|\bar{E}_z|} \tag{4}$$

where m is the electron mass, $(\gamma_{inj} - 1)mc^2$ is the energy of the beam upon injection, and $(\gamma_f - 1)mc^2$ is the final energy of the particles as they exit from the beam. Note that unless the beam is fully neutralized by the plasma channel (f = 1) the propagating gamma of the beam, γ_o, is less than γ_{inj}:

$$\gamma_{inj} = \gamma_o + \gamma_U \tag{5}$$

where $\gamma_U mc^2$ is the field potential energy:

$$\gamma_U = \frac{eI_b L_b (1 - f)}{mc^3} . \tag{6}$$

Here, $L_b = 2\log(r_w/r_b)$ is a dimensionless inductance and r_b is the beam radius. Note that for the vacuum case (f = 0) the above gives the familiar expression for the limiting current of a beam with $\gamma = \gamma_U$ propagating in a drift tube of radius r_w. Using Eqs. (3), (4) and (5), the erosion rate may be written in terms of equilibrium beam and channel parameters, β_p and γ_f:

$$\beta_o - \beta_p = \frac{efI_b L_c \beta_p}{mc^3(\gamma_o + \gamma_U - \gamma_f)} . \tag{7}$$

The value of γ_f can be estimated via a simple argument. In the case where Eq. (7) holds, the erosion process establishes a constant velocity for the pinch point, $v_p = \beta_p c$. Assuming the energy of the beam is lost to

the E_z spike adiabatically, a particle with a velocity infinitesimally less than v_p will fall behind the pinch region, where the E_z spike is localized. The final velocity of this beam particle, v_f, is therefore approximated by

$$\beta_p = \beta_f = (1 - \frac{1}{\gamma_f^2})^{1/2} \simeq 1 - \frac{1}{2\gamma_f^2} \tag{8}$$

Substituting β_p from (8) into (7), we obtain a cubic equation which determines γ_f:

$$\gamma_f^3 - (\gamma_o + \gamma_U + 2C\gamma_o^2)\gamma_f^2 - \gamma_o^2\gamma_f + (\gamma_o + \gamma_U + C)\gamma_o^2 = 0 \tag{9}$$

where

$$C = \frac{efI_bL_c}{mc^3} . \tag{10}$$

To verify the theoretical inductive erosion rates predicted by Eq. (7), simulations with FRIEZR were performed over a range of values for the beam current, I_b = 2-10 kA, and the plasma ionization fraction, f = 0.2-1.0, with γ_o = 10. The beams generally showed the characteristic trumpet shape as expected, but also had features that were not accounted for in the simple model that produced Eq. (7), such as the multiple E_z spikes that were observed at high I_b and f values. In these cases, oscillatory behavior at the beam head was characteristic of the relativistic electron-electron two-stream instability.

In the relativistic limit, where the beam electrons have longitudinal and transverse effective masses which differ significantly, the fastest growing mode of the two-steam instability is characterized by a wave vector that is not parallel to the direction of propagation. Here, we consider a cold beam interacting with a cool plasma of density n_c, where n_c is the

channel electron density. Typically[6,2] the fastest growing wave vector features $k_{\parallel} = \omega_c/v_b$ and $k_{\perp} = k_r \simeq r_b^{-1}$, where $\omega_c^2 = 4\pi n_c e^2/m$ and r_b^{-1} is taken to be the lowest available $k_{\perp}$. Because we are constrained by axisymmetry, $k_{\theta} = 0$, giving the mode a sausage-like structure in r and ζ. Results of a FRIEZR run in which these oscillations were observed are shown in Fig. 1. The plot of E_z versus ζ on axis shows the oscillations and corresponding plot of $R_{1/2}$, the radius within which one-half of the initial beam current is enclosed at a given ζ, shows the sausage structure of the instability. Note that in the figures, the beam is moving to the left. Note also that the beam has been assigned a positive charge so that $E_z < 0$ is decelerating. As can be seen in the figures, the oscillatory behavior is confined to the beam head, where the channel electrons have not yet been fully ejected. This means that over the length of the interaction region, the channel electron density is dropping from its peak initial value to zero. In this run, $I_b = 5$ kA, $r_b = 1$ cm, $r_c = 2$ cm and $f = 1$. With these parameters, the initial average channel electron density is $n_c = 8.3 \times 10^{10}$ cm^{-3} so that the oscillations will have an initial wavelength of $\lambda_c = 11.6$ cm which increases as the channel density drops. The three distinct peaks in the E_z plot of Fig. 1 show increasing separation consistent with this scenario. Channel electron and beam electron densities on axis are also plotted in Fig. 1. Note that the oscillations in E_z and $R_{1/2}$ correspond to oscillations in n_c. Note also that the n_c and n_b plots show the value on axis, rather than the lower average value in the channel. Because the values of all parameters are changing over the course of each oscillation wavelength, the instability does not lend itself to a more detailed analysis. It is of interest, however, that this phenomena is confined to the beam head and, as we shall see below, does not adversely affect the argument that produced Eq. (7).

Beam head erosion is ideally measured from simulation results by observing the movement of the pinch point, as a function of time, to larger ζ values, where $\zeta = ct - z$. In the presence of the complicated beam head dynamics discussed above, however, the location of the pinch point is sometimes difficult to define. In all cases, we looked at a number of features, but the most reliable measurement has proven to be I_{encl} versus ζ, where I_{encl} is defined to be the current enclosed inside the radius $r = 5\ r_b$. Examples of this diagnostic are given in Figs. 2 and 3. Figure 2 shows superimposed plots of I_{encl} versus ζ at $c\tau = 5$ meters and 10 meters for the beam pictured in Fig. 1. The superimposed plots give a reasonable measurement of the erosion rate, despite the dynamics at the beam head. Figure 3 is a similar superposition of I_{encl} versus ζ plots at $c\tau = 30$ and 40 meters. The parameters are $I_b = 2$ kA, $f = 0.2$, $r_b = 1$ cm and $r_c = 2$ cm. Corresponding plots of E_z, $R_{1/2}$, n_b and n_c versus ζ (see Fig. 4) show that this beam lacks the instabilities seen in Fig. 1, having a well defined pinch point and E_z spike. In such cases, these other features corroborated the erosion rate estimated from the I_{encl} plots.

Erosion rates for various values of I_b and f are shown in Table 1. In all cases, $\gamma_o = 10$, $r_b = 1$ cm, $r_c = 2$ cm, $r_w = 33$ cm, ζ_r (beam rise length) = 50 cm, and $\zeta_{max} = 100$-400 cm. The erosion rate predicted by Eq. (7) is also given. These rates were seen to be insensitive to the channel radius, as expected, and additional runs at $I_b = 10$ kA and $f = 0.2$ showed correct scaling with γ_o and with r_w. It is interesting that the results agree so closely with theory, even when the beam dynamics are complicated. It is also true, however, that as long as the energy losses are confined to the beam head, as in these cases, the energy balance argument that produced Eq. (7) still applies.

It is important to note that Eq. (7) differs from previous analyses mainly in the treatment of γ_f, which is calculated by solving Eq. (9). A common feature of previous treatments[2] of inductive erosion in this regime is to assume either $\gamma_o >> \gamma_f$ or $\gamma_f = 1$. It is easy to see that, for our I_b = 2 kA cases, either of these approximations will cause the erosion rate to be underestimated by as much as 50%, because the particle dynamics limit the amount of energy that can be extracted from the beam. Another consequence of these dynamics is that a population of particles with $\gamma = \gamma_f$ may remain behind the beam head. In those cases where γ_f is large, as in the I_b = 2 kA cases, a significant portion of these particles may remain at small radii, near the beam, and will show up in the I_{encl} plots as an apparent current enhancement behind the beam head (see Fig. 3). Because these particles are behind the pinch region, they are an artifact with no effect on the beam head dynamics.

III. Emittance Driven Erosion

For a beam propagating in near-equilibrium, transverse emittance losses are confined to the beam head, where the pinch force is not sufficient for confinement. In cases where this is the dominant erosion mechanism, the loss of particles in the radial direction causes the length scale for pinching to increase so that an increasing portion of the beam is susceptible. One expects these losses to be significant only when the pinch force and inductive E_z spike at the head of the beam are weak, as in the case of low current. When considering the decrease in the erosion rate as the current is lowered, emittance losses would appear to place a lower bound on the erosion rate given by Eq. (7).

This issue was recently addressed in this regime by Buchanan,[7] who employed the envelope equations of Lee and Cooper,[7] which require that the

radial profile of the beam be a function that is parameterized by $R(\zeta,z)$, the root mean square radius. This radial function is specified and $R(\zeta,z)$ is solved for. In Buchanan's analysis, a Gaussian profile was used. The resulting equations could not be solved analytically, but the lack of an equilibrium solution (characterized by $\partial/\partial z = 0$) was demonstrated, indicating a nonzero erosion rate for all time. When the equations were solved numerically for a wide range of parameters it was found that the asymptotic erosion rate is a constant given by empirical expression

$$\beta_o - \beta_p = 0.18 \frac{1}{\sqrt{\gamma_o}} \left(\frac{r_b}{r_c}\right)^{2(1+f)} f^{0.9} \quad . \tag{11}$$

This was addressed independently by Nguyen and Uhm,[8] who again applied the envelope equations of Lee and Cooper to a beam with a Gaussian radial profile. They made the additional assumption that, after a short transient, *the erosion rate is constant and the axial profile of the beam* is fixed so that all relevant qualities vary only as $X = v_p t - z$, where v_p is the velocity of the eroding pinch point. As above, the envelope equations were solved numerically with resulting erosion rates summarized by the expression:

$$\beta_o - \beta_p = \frac{1}{\sqrt{\gamma_o}} \left(\frac{r_b}{r_c}\right)^3 \times \begin{cases} 0.094\ f^{0.85} & f > 0.1 \\ 0.044\ f^{0.5} & f < 0.1 \end{cases} \quad . \tag{12}$$

From Eq. (7) and Eqs. (11) and (12) we expect that emittance erosion should not contribute significantly to losses in high current beams, which is apparently the case for the parameters used in Table 1. At low current (< 1 kA) and high γ_o (> 20), however, these equations suggest that significant effects should be observable in the simulations.

We investigated this possibility by making several runs with I_b = 1 kA, γ_o = 20, ζ_r = 10 cm, ζ_{max} = 100-400 cm. The values used for the ionization fraction, $0.055 \leq f \leq 1.0$, and the ratio of beam to channel radius, $1.0 \leq r_b/r_c \leq 3.0$, were chosen so as to satisfy two conditions: (1) we require $n_c \leq n_b$ throughout the channel so that all channel electrons will be expelled and (2) the predicted emittance erosion rate must dominate over the inductive effects. From Eqs. (11) and (12) erosion rates ranging from $\beta_o - \beta_p < 0.01$ up to $\beta_o - \beta_p > 0.08$ were expected for these parameters.

As in the inductive cases, erosion was measured from plots of I_{encl} versus ζ once steady-state erosion was established. In contrast with the inductive case, where this could be determined from the average particle energy in the beam head, we had to rely on axial profiles of beam quantities to indicate steady-state, or near steady-state behavior. In all cases, we found erosion rates of $.01 < \beta_o - \beta_p < .03$, which varied only sluggishly with f and r_b/r_c. The measured rates also varied with the numerical parameters, $\Delta\zeta$ and $\Delta\tau$, indicating that the erosion rates were less than or of the order of the numerical errors.

To clarify these data, we repeated several of the runs with γ_o = 5. This reduction in γ_o should double the rate of emittance erosion, according to (11) and (12). Inductive erosion effects were removed in these cases by specifying $E_z = 0$ in the part of the simulation where the beam particles are acted on by the fields (the particle push routine). In all cases, we found $\beta_o - \beta_p \approx 0.005$, a reduction in the erosion rate that is opposite the scaling predicted in (11) and (12). Because the measurements were made in the asymptotic limit as required to obtain steady state behavior, we concluded that the rate of erosion due to the finite emittance of the beam

tends toward zero in the asymptotic limit. This conclusion is supported by further analysis of the simulations.

To further investigate the results, the beam was diagnosed for average transverse emittance as a function of ζ throughout the simulation. Plots of I_{encl} versus ζ from a run in which $\gamma_o = 5$, $f = 1$, $r_b = r_c = 2$ cm, $I_b = 1$ kA and in which $E_z = 0$ were specified in the particle push routine as shown in Fig. 5. Early in the simulation, at $c\tau = 4$ meters, the initial rise length of 10 cm has increased to 100 cm, and a low emittance population of particles, with $T < T_o/2$, has developed at the beam head, where T_o is the initial transverse temperature of the beam. Beyond $c\tau = 4$ meters, the axial profile evolves slowly, with both the rise length and the low-emittance population continuing to increase and the rate of increase in these quantities tending toward zero. Note that because of the low energy, $\gamma_o = 5$, $\beta_o = 0.98$, the beam motion relative to the coordinates will be discernible over the course of the simulation, which continues until $c\tau = 40$ meters. This motion can be seen in the the $c\tau = 4$ m and $c\tau = 40$ m plots of Fig. 5. When measuring the cumulative effects of the transient erosion process over a long distance, this must be taken into account.

The progress toward an asymptotic state can be seen in Fig. 6, where the growth of the low emittance population is shown by plotting ζ_T versus z, where ζ_T is the coordinate of the point at which the beam particles have transverse temperature $T = T_o/2$ and $z = c\tau$. Particles with $\zeta < \zeta_T$ will have lower emittance. As the beam reaches an asymptotic state, the motion of $\zeta_T(z)$ will match the motion of the beam body, $\zeta_b(z) = (1 - \beta)z$, so that $\zeta_T(z)$ and $\zeta_b(z)$ will have the same slope. A line with slope $d\zeta/dz = 1 - \beta$ is also plotted in Fig. 6. Note that for $z \gtrsim 20$ m the two slopes have converged to within numerical fluctuations.

The result of an asymptotically vanishing erosion rate is clearly a departure from the predictions of Eqs. (13) and (14). The discrepancy resides in the assumption of self-similar radial structure which is fundamental to the derivation of the envelope equations. This assumption appears to be too limiting in this case, where the beam must be parameterized, at the very least, by $T(\zeta,z)$ as well as $R(\zeta,z)$. The beam may in fact assume a highly non-Gaussian profile at early times, when high temperature particles escape and low temperature particles remain trapped by the weak pinch potential. These trapped particles contribute to the increased rise length of the beam.

IV. Conclusions

We have seen that numerical simulations of inductive erosion agree closely with the theory over a wide range of parameters, even when the beam dynamics are complicated by unstable behavior in the beam head. These results demonstrate that at low energies (< 5 MeV) careful consideration of the relativistic dynamics of the beam particles are required for accurate prediction of inductive erosion rates. This, in effect, limits ones ability to reduce the erosion rate by various means because a lower erosion rate results in a higher γ_f. At higher energies, the $\gamma_o >> \gamma_f$ approximation holds, and our results are in agreement with previous formulations.[2]

In the case of emittance erosion, simulations indicate that a steady-state erosion rate is not established and that the radial expansion at the beam head is not self-similar, thereby departing from previous theoretical assumptions.[2,8] As the beam-channel equilibrium is established, these beams develop a long rise length of low-emittance particles, with an erosion rate that tends towards zero. Because the simulations show that

this asymptotic behavior establishes itself only over large propagation distances, this may not be easily observable in laboratory cases of interest. For these cases a new analysis, in which the radial dynamics are treated more carefully, would be required.

Acknowledgments

We are happy to acknowledge many helpful and stimulating discussions with M. Mostrom of Mission Research Corporation.

This work was supported by the Defense Advanced Research Projects Agency, under contract number N60921-86-WR-W0233.

Appendix

For these studies we have used an electromagnetic particle simulation code, FRIEZR, which was written to study the propagation of high energy electron beams in the Ion Focus Regime in an axisymmetric coordinate system. The elements of the code are beam and plasma electrons which are treated as particles, and plasma ions which may be treated as an immobile background. The code is written in a transformed coordinate system (r,ζ,τ), where $\zeta = ct - z$ and $\tau = t$. For a highly relativistic beam, the axial variable, ζ, measures distance behind the beam head. The beam moves slightly slower than c so the beam head slips slowly backward in the coordinate system, but for high energy beams and short propagation distances, the slippage is not significant relative to the size of the simulation region. The particle dynamics are determined from the solution of Maxwell's equations written in the (r,ζ,τ) variables with current and charge densities determined from the simulation particles. We write the equations for the vector and scalar potentials, $\vec{A}$ and ϕ, in a gauge suggested by Lee which is particularly convenient for axisymmetry.[9] In this gauge, which has the condition

$$\nabla_\perp \cdot \vec{A}_\perp = 0 \ , \tag{A1}$$

we may write the parallel and perpendicular components of Ampere's law as

$$\nabla_\perp^2 \left(\frac{\partial A_z}{\partial z} + \frac{1}{c} \frac{\partial \phi}{\partial t} \right) = \frac{4\pi}{c} \nabla_\perp \cdot \vec{J}_\perp \tag{A2}$$

and

$$\nabla_\perp^2 A_z + \frac{1}{c} \frac{\partial E_z}{\partial t} = - \frac{4\pi}{c} J_z \ . \tag{A3}$$

We change variables to the $(r,\zeta=ct-z,\tau=t)$ coordinate system and write

$$\nabla_\perp^2\left(-\frac{\partial a}{\partial \zeta} + \frac{1}{c}\frac{\partial \phi}{\partial \tau}\right) = \frac{4\pi}{c}\nabla_\perp \cdot \vec{J}_\perp \tag{A4}$$

and

$$\nabla_\perp^2(a + \phi) + \left(\frac{1}{c}\frac{\partial}{\partial \tau} + \frac{\partial}{\partial \zeta}\right)E_z = -\frac{4\pi}{c}J_z \ , \tag{A5}$$

where

$$a = A_z - \phi \tag{A6}$$

and

$$E_z = -\left(\frac{1}{c}\frac{\partial}{\partial \tau} + \frac{\partial}{\partial \zeta}\right)a - \frac{1}{c}\frac{\partial \phi}{\partial \tau} \ . \tag{A7}$$

Using the continuity equation,

$$\nabla_\perp \cdot \vec{J}_\perp - \frac{\partial J_z}{\partial \zeta} + \frac{\partial \rho}{\partial \tau} + c\frac{\partial \rho}{\partial \zeta} = 0 \ , \tag{A8}$$

and Gauss' law,

$$\nabla_\perp^2 \phi + \frac{\partial E_z}{\partial \zeta} = -4\pi\rho \ , \tag{A9}$$

we may write equations (A4) and (A5) as

$$\nabla_\perp^2\left(-\frac{\partial a}{\partial \zeta} + \frac{1}{c}\frac{\partial \phi}{\partial \tau}\right) = \frac{4\pi}{c}\left(\frac{\partial J_z}{\partial \zeta} - \frac{\partial \rho}{\partial \tau} - c\frac{\partial \rho}{\partial \zeta}\right) \tag{A10}$$

and

$$\nabla_\perp^2 a + \frac{1}{c}\frac{\partial E_z}{\partial \tau} = \frac{4\pi}{c}(\rho c - J_z) \ . \tag{A11}$$

In axisymmetry, $A_r = 0$ and the A_θ equation is decoupled from the a and ϕ equations, so that

$$\nabla^2 A_\theta - \frac{A_\theta}{r^2} - \frac{1}{c}\frac{\partial}{\partial\tau}\left(\frac{1}{c}\frac{\partial}{\partial\tau} + 2\frac{\partial}{\partial\zeta}\right)A_\theta = -\frac{4\pi}{c}J_\theta \ . \qquad \text{(A12)}$$

These equations determine the dynamics of the system and are solved at each time step to determine the potentials from the charge and current densities. The electric and magnetic fields are then obtained from the potentials in the usual way. The field equations are differenced implicitly in both the radial and axial directions, but an alternate version with explicit differencing in the axial direction has also been used. Once the fields are calculated, the code pushes all particles relativistically in Cartesian coordinates using standard techniques. In order to determine the densities, we use a particle lay-down scheme which is quadratic in the radial direction and linear (or Nearest Grid Point in the alternate version) in the axial direction. The code should be valid for moderate energy as well as high energy beam propagation studies.

References

1. G. J. Caporaso, F. Rainer, W. E. Martin, D. S. Prono and A. G. Cole, Phys. Rev. Lett. 57, 1591 (1986).

2. H. L. Buchanan, Phys. Fluids 30, 221 (1987) and references within.

3. W. M. Sharp and M. Lampe, Phys. Fluids 23, 2383 (1980).

4. K. T. Nguyen, R. F. Schneider, J. R. Smith and H. S. Uhm, Appl. Phys. Lett. 50, 239 (1987).

5. M. A. Mostrom, D. Mitrovich, B. B. Godfrey, D. R. Welch and R. M. Clark, Bull. Am. Phys. Soc. 33, 1883 (1988).

6. S. A. Bludman, K. M. Watson and M. N. Rosenbluth, Phys. Fluids 3, 747 (1960).

7. E. P. Lee and R. C. Cooper, Particle Accelerators 7, 83 (1976).

8. K. T. Nguyen and H. S. Uhm (private communication).

9. W. S. Sharp, S. S. Yu and E. P. Lee, L.L.N.L. Report UCID-21114 (unpublished, 1987).

Table 1. Erosion rates from simulation results and corresponding values predicted by Eq. (7).

I_b (kA)	f	$\beta_o-\beta_p$ (FRIEZR)	$\beta_o-\beta_p$ [Eq. (7)]
2	0.2	0.024	0.022
2	0.5	0.039	0.046
2	1.0	0.094	0.084
5	0.2	0.043	0.040
5	0.5	0.085	0.090
5	1.0	0.16	0.17
10	0.2	0.061	0.062
10	0.5	0.15	0.14
10	1.0	0.28	0.26

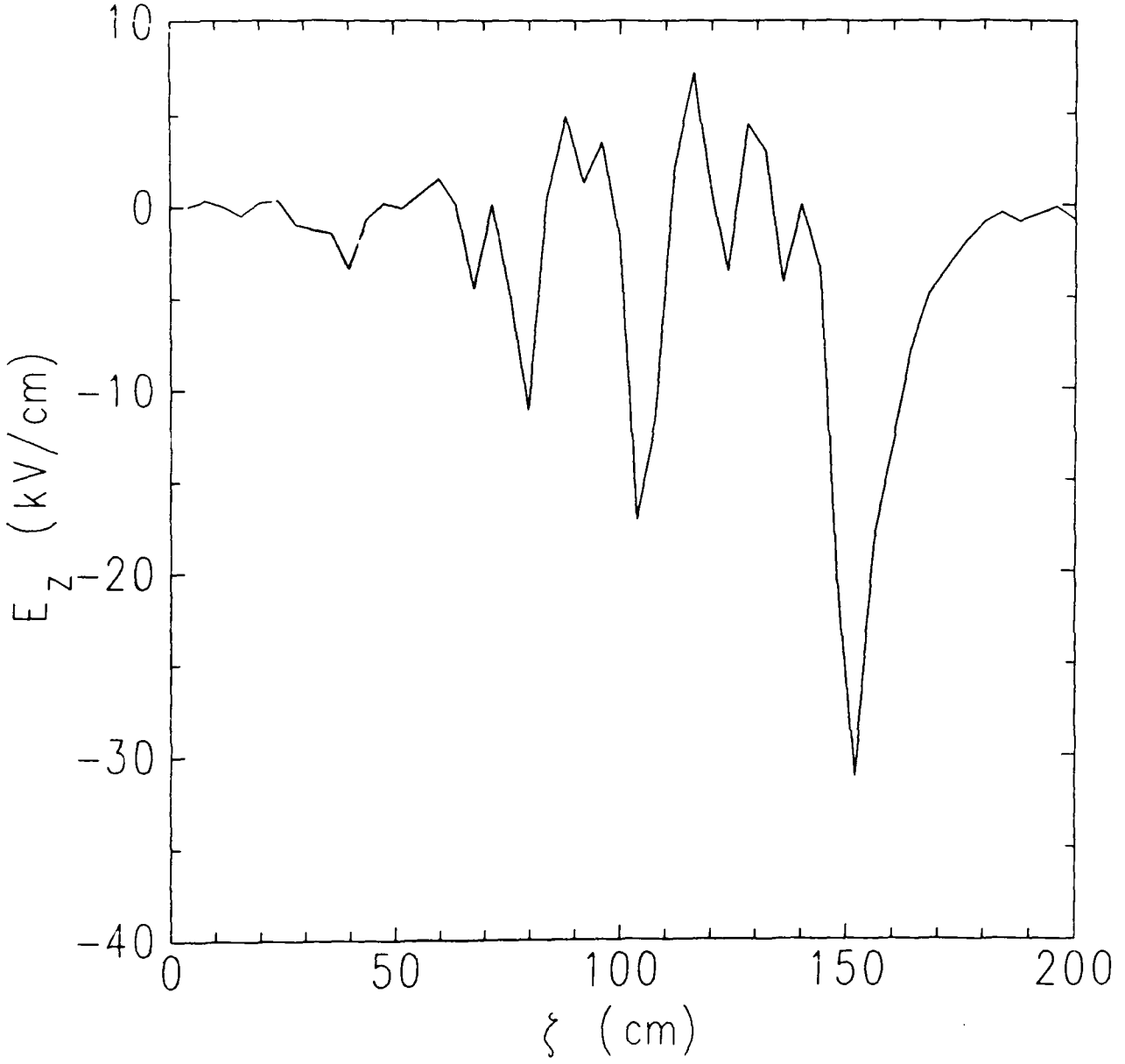

Fig. 1 — E_z vs ζ, $R_{1/2}$ vs ζ, and n_e and n_b vs ζ are plotted separately at $c\tau$ = 7 meters for a beam with parameters: I_b = 5 kA, f = 1.0, λ_o = 10, r_b = 1 cm, r_c = 2 cm and r_w = 33 cm

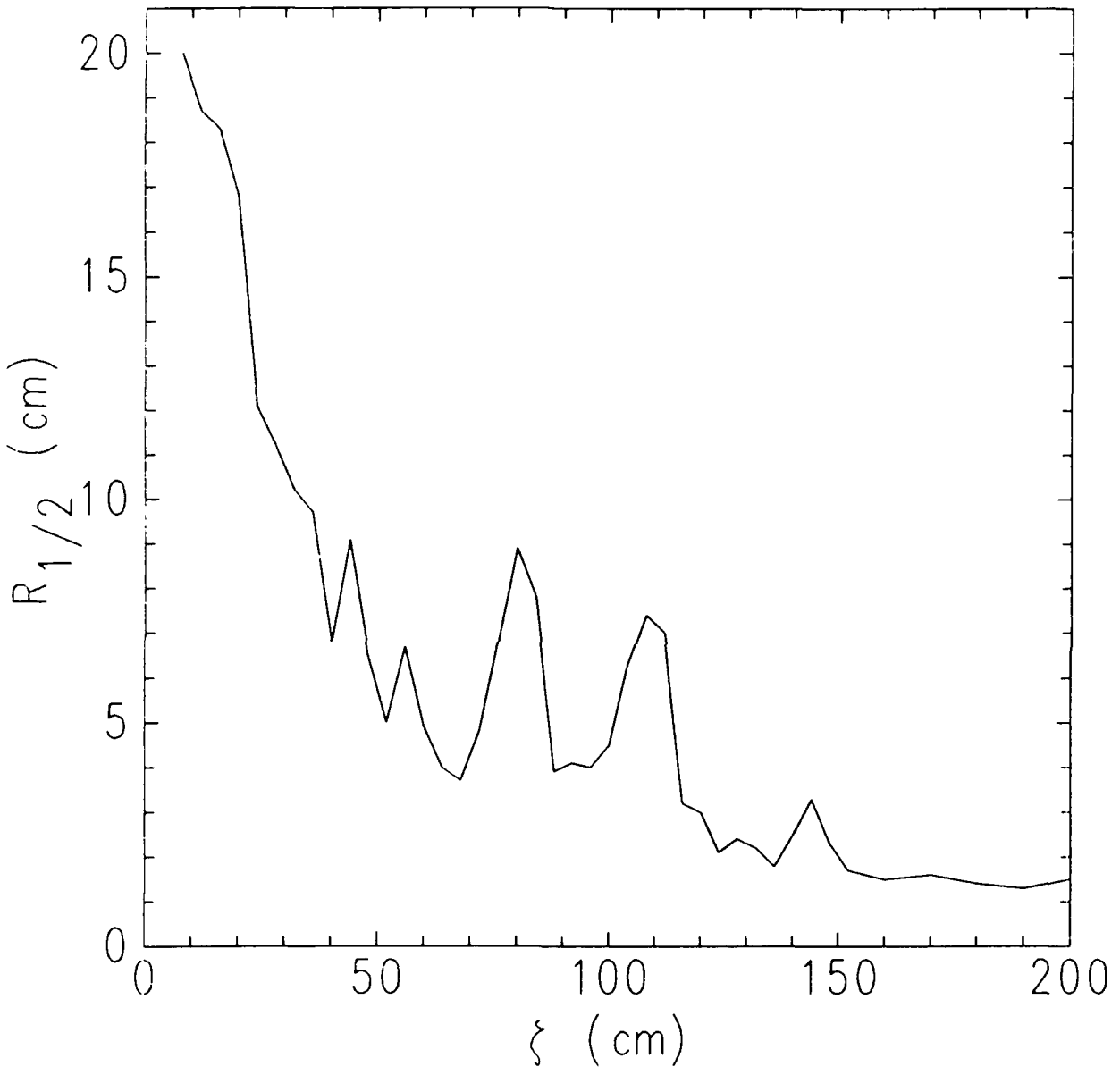

Fig. 1 — (Continued) E_z vs ζ, $R_{1/2}$ vs ζ, and n_e and n_b vs ζ are plotted separately at $c\tau$ = 7 meters for a beam with parameters: I_b = 5 kA, f = 1.0, λ_{zz} = 10, r_b = 1 cm, r_c = 2 cm and r_w = 33 cm

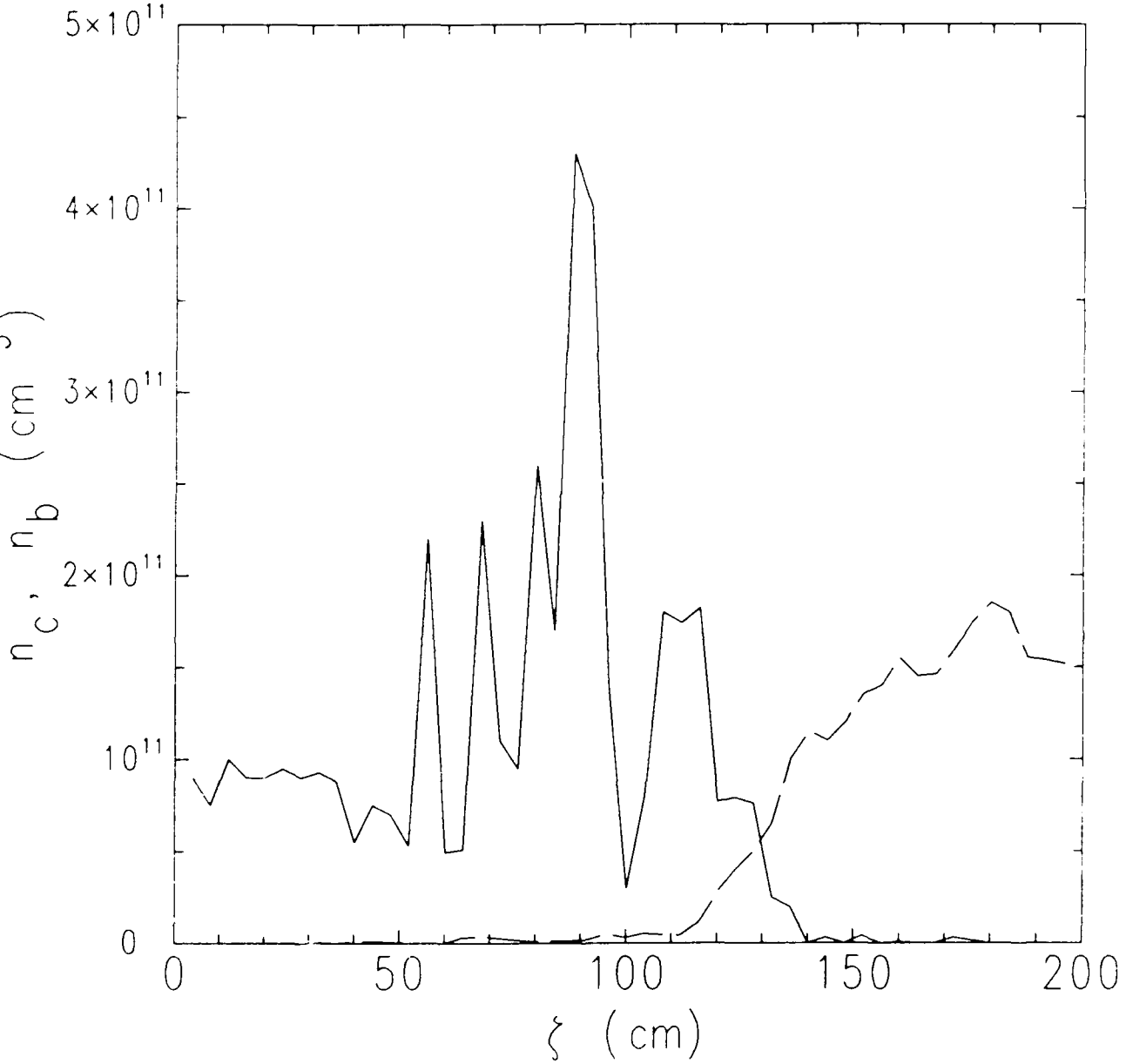

Fig. 1 — (Continued) E_z vs ζ, $R_{1/2}$ vs ζ, and n_c and n_b vs ζ are plotted separately at $c\tau$ = 7 meters for a beam with parameters: I_b = 5 kA, f = 1.0, λ_{μ} = 10, r_b = 1 cm, r_c = 2 cm and r_w = 33 cm

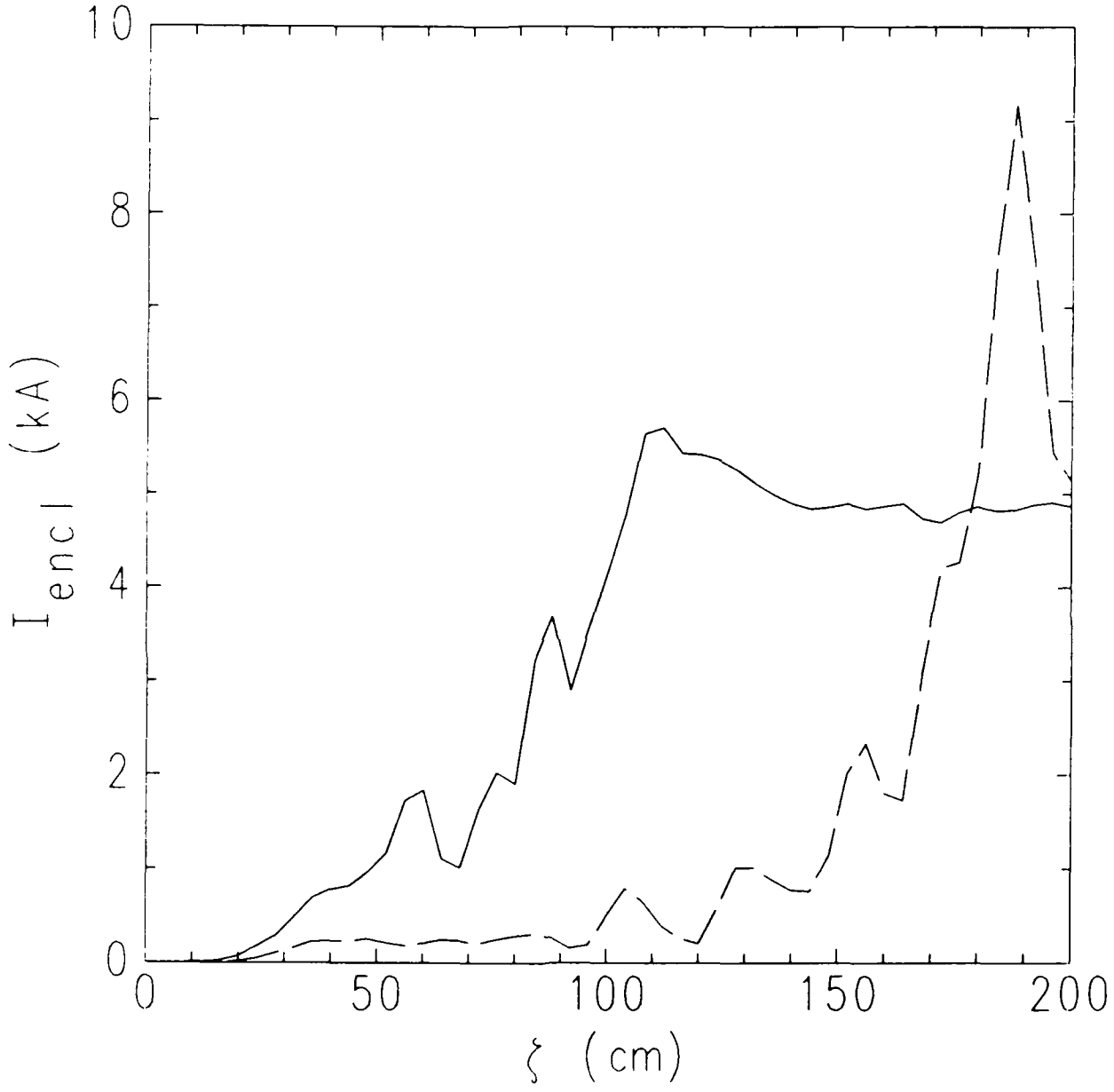

Fig. 2 I_{encl} vs ζ plots overlayed for $c\tau$ = 5 meters (solid) and 10 meters (dashed) show erosion of the current. I_{encl} is the total current within $r = 5r_b$. Here, parameters are the same as for Fig. 1. Such plots were used to measure the erosion rates given in Table 1.

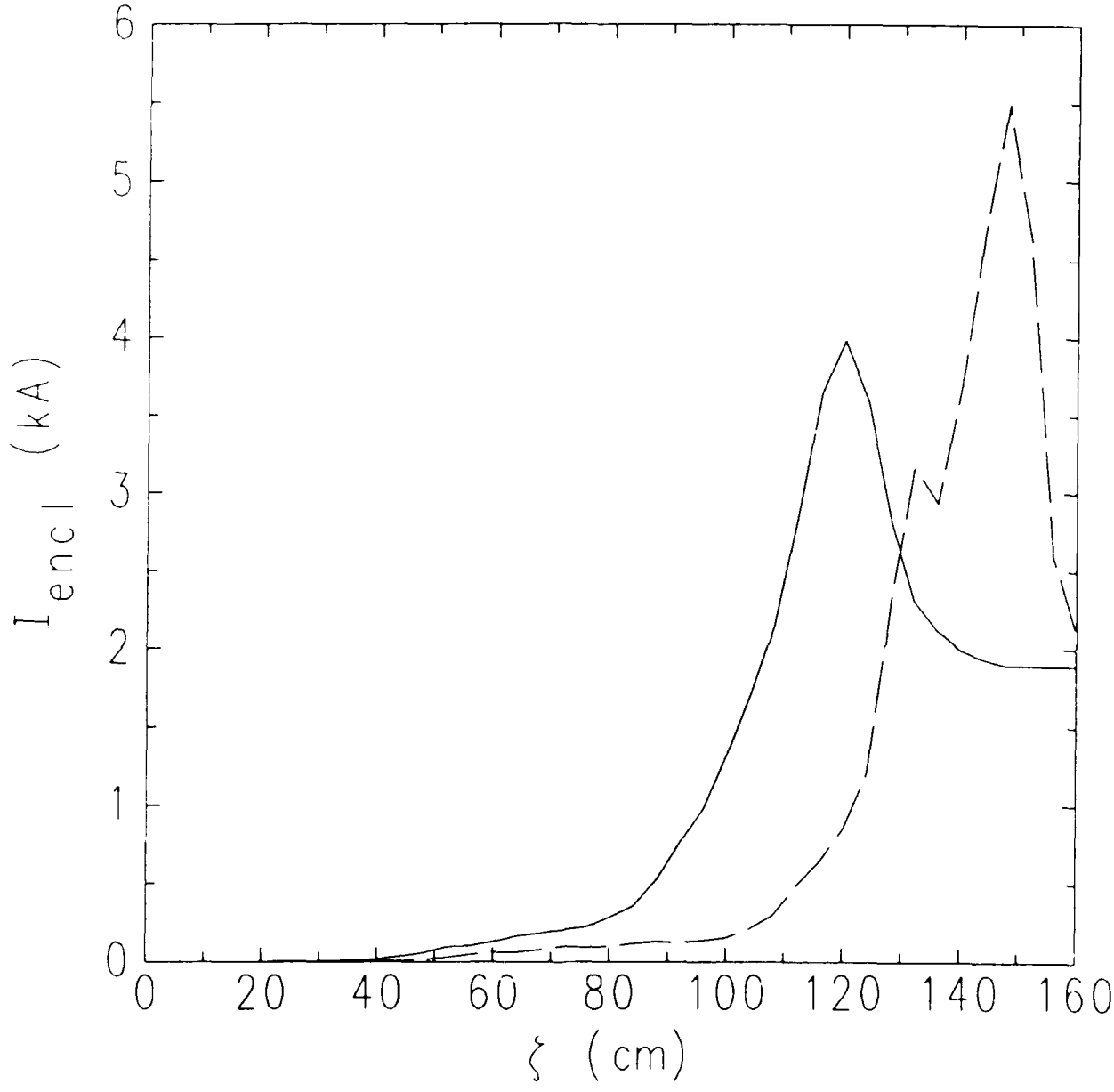

Fig. 3 — I_{encl} vs ζ plots are overlayed for $c\tau$ = 30 meters (solid) and 40 meters (dashed) for a beam with parameters: I_b = 2 kA, f = 0.2, λ_z = 10, r_b = 1 cm, r_s = 2 cm and r_w = 33 cm.

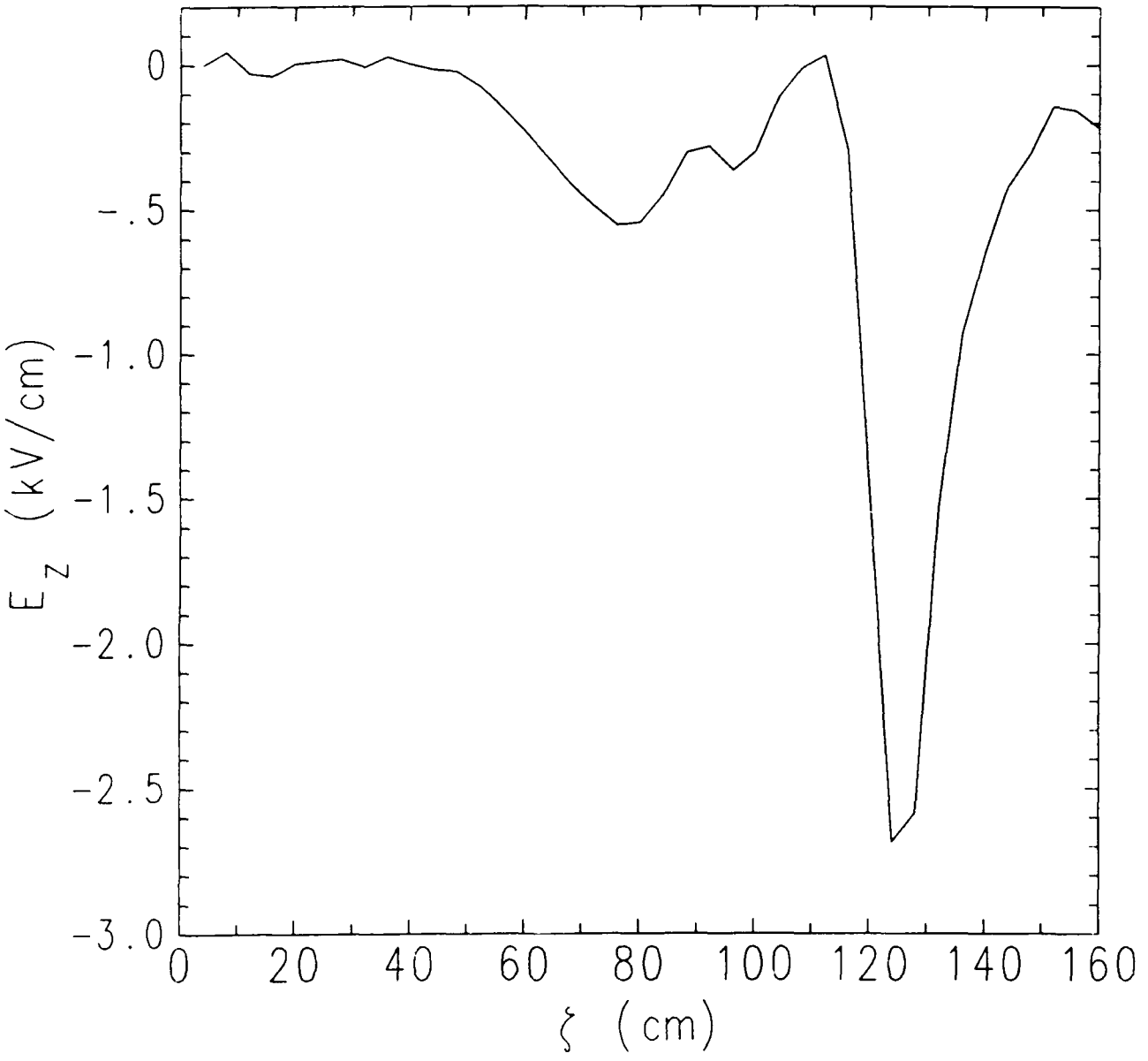

Fig. 4 — E_z vs ζ, $R_{1,2}$ vs ζ, and n_i and n_b vs ζ are plotted separately at $c\tau$ = 30 meters. The parameters are the same as in Fig. 3.

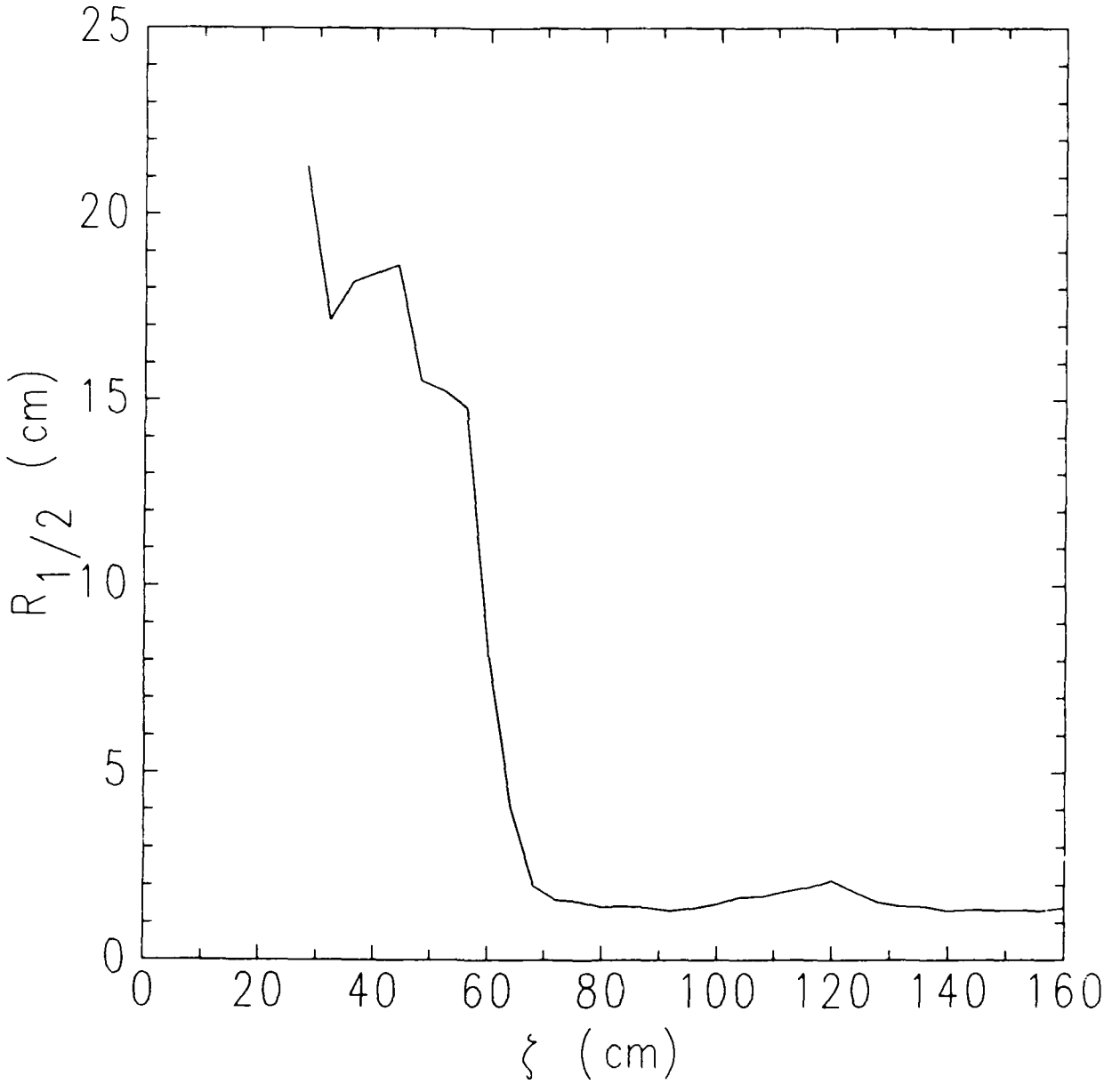

Fig. 4 — (Continued) E_z vs ζ, $R_{1/2}$ vs ζ, and n_e and n_b vs ζ are plotted separately at $c\tau$ = 30 meters. The parameters are the same as in Fig. 3.

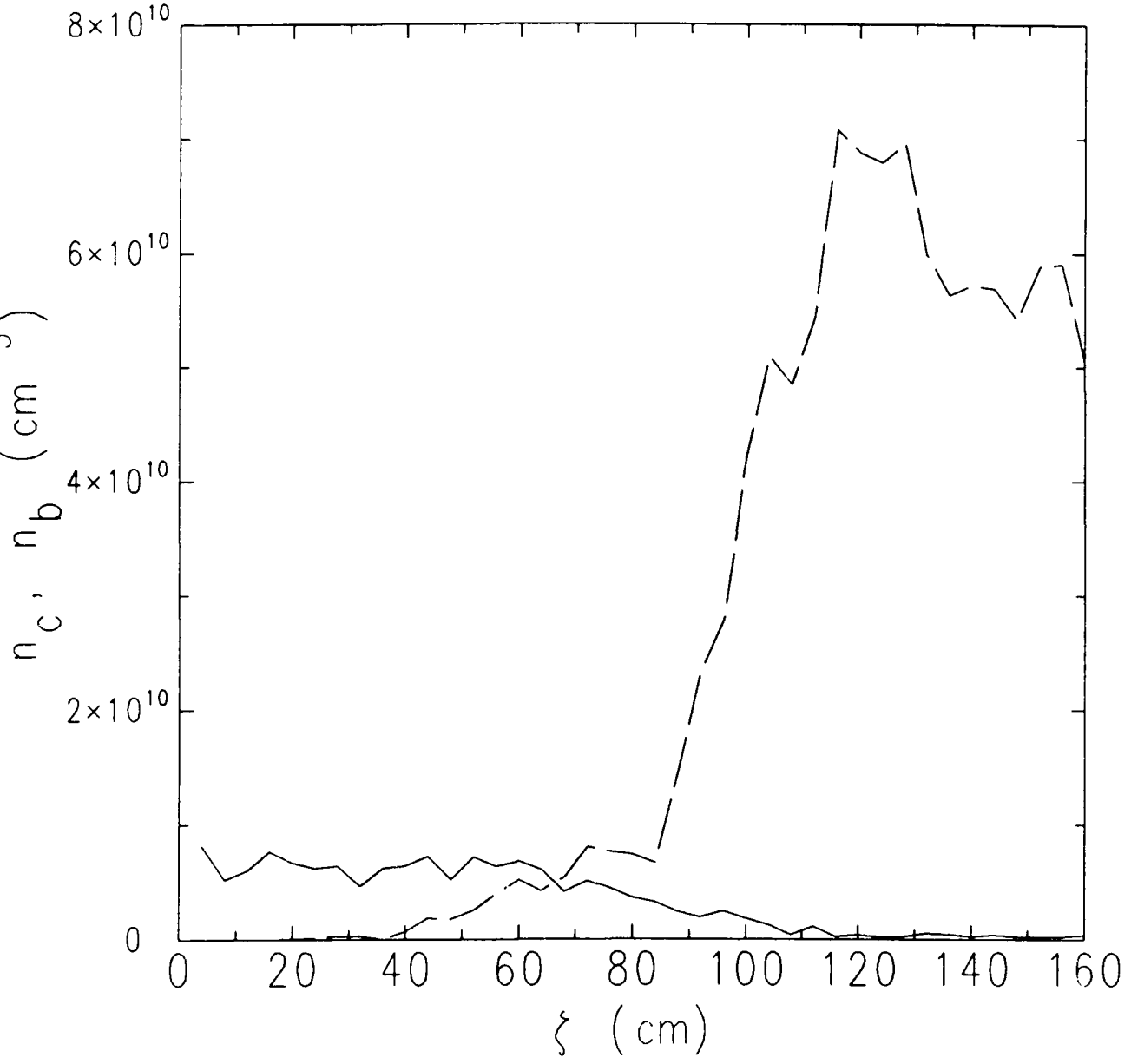

Fig. 4 — (Continued) E_z vs ζ, $R_{1/2}$ vs ζ, and n_e and n_b vs ζ are plotted separately at $c\tau$ = 30 meters. The parameters are the same as in Fig. 3.

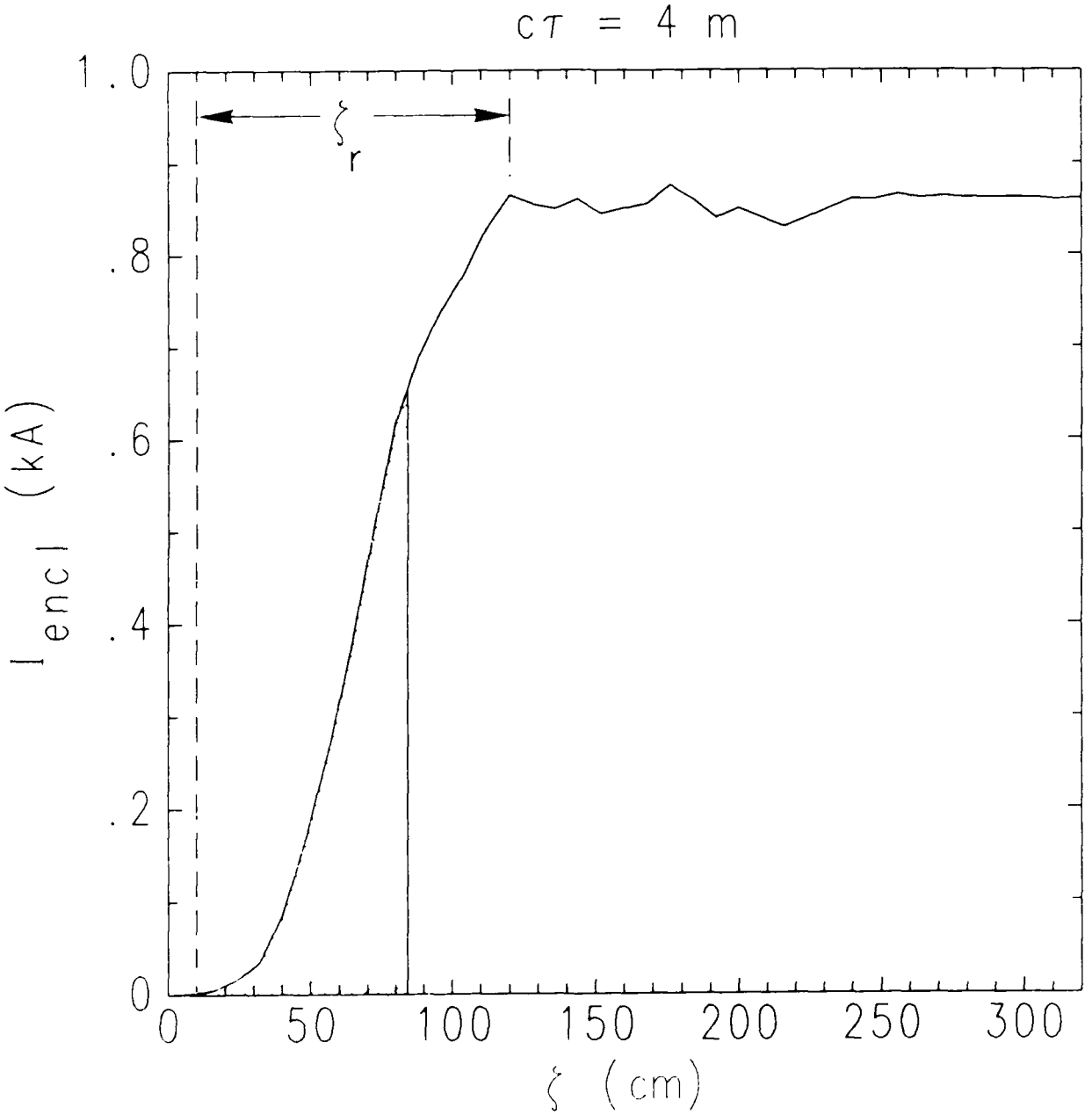

Fig. 5 — I_{encl} vs ζ plotted at $c\tau$ = 4 and 40 meters shows an increase in the rise length, ζ_r, and the development of a low-emittance population at the beam head. Areas with low transverse temperature, $T < T_{\perp}/2$, are shaded. Parameters are I_b = 1 kA, f = 1, λ_o = 5 and $r_b = r_c$ = 2 cm. E_z = 0 is specified in the particle push routine.

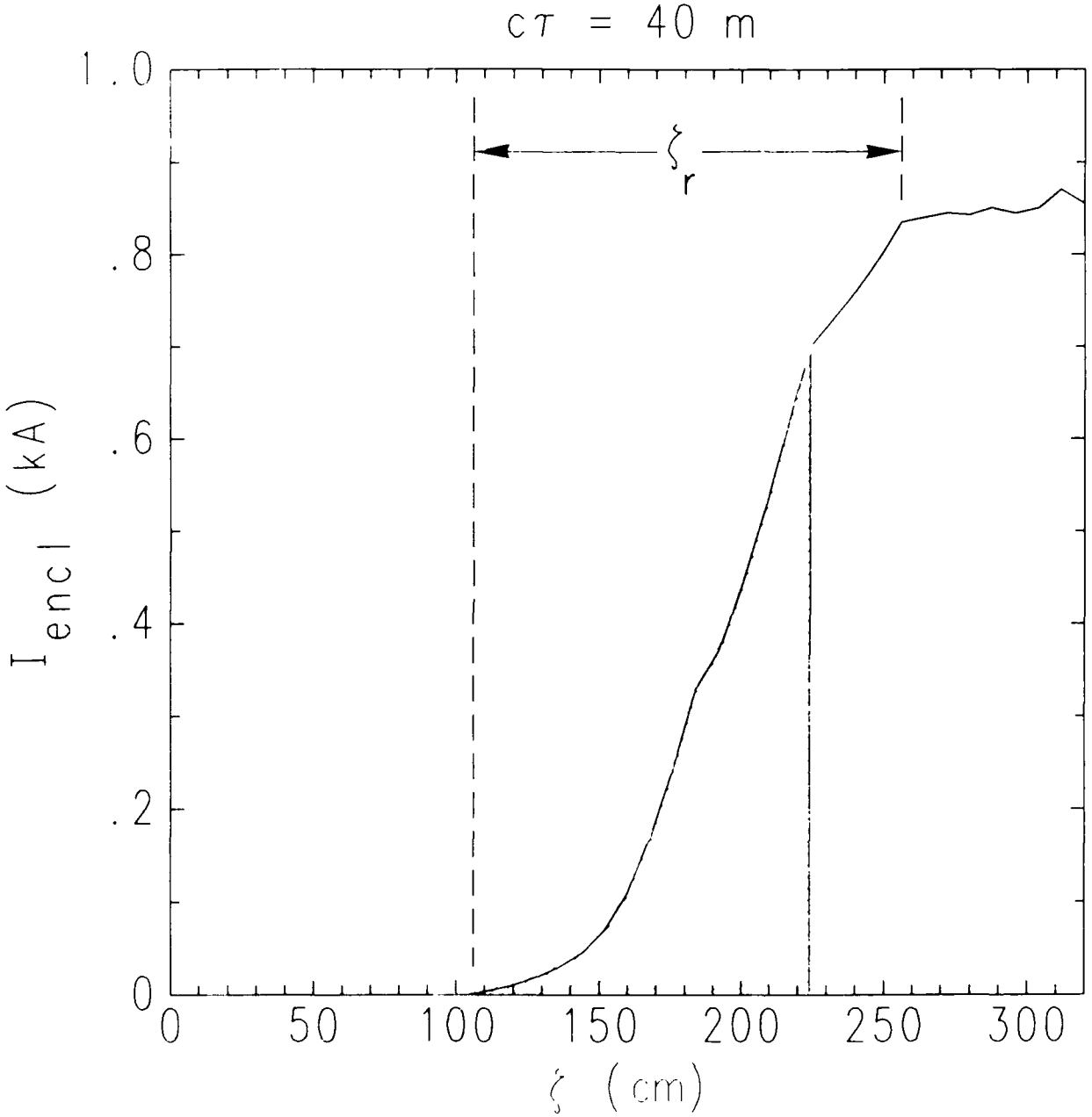

Fig. 5 — (Continued) I_{encl} vs ζ plotted at $c\tau$ = 4 and 40 meters shows an increase in the rise length, ζ_r, and the development of a low-emittance population at the beam head. Areas with low transverse temperature, $T < T_0/2$, are shaded. Parameters are I_b = 1 kA, f = 1, λ_0 = 5 and $r_b = r_c$ = 2 cm. E_z = 0 is specified in the particle push routine.

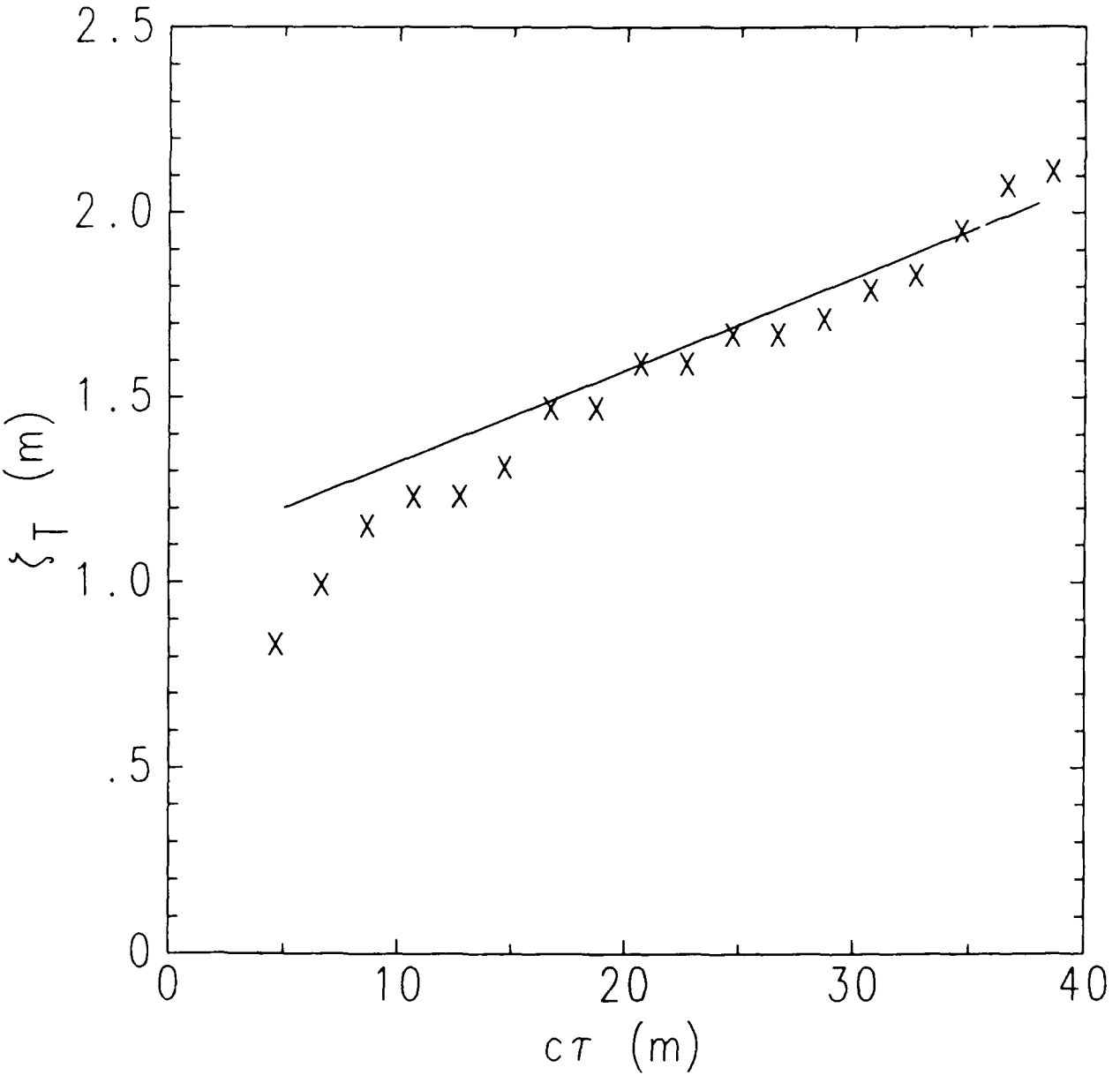

Fig. 6 — The coordinate location of the $T = T_0/2$ point, ζ_T, is plotted vs $c\tau$ for the simulation pictured in Fig. 5. As the asymptotic near-equilibrium state is reached, this point will become stationary with respect to the beam body, attaining a slope $d\zeta_T/dz = d\zeta_b/dz = 1 - \beta$, where $d\zeta_b/dz$ is the velocity of the beam body relative to the simulation coordinate frame and $z = c\tau$. A line with slope $1 - \beta$ is also plotted.

Distribution List*

Naval Research Laboratory
4555 Overlook Avenue, S.W.
Attn: CAPT W. G. Clautice - Code 1000
Dr. M. Lampe - Code 4792 (20 copies)
Dr. T. Coffey - Code 1001
Head, Office of Management & Admin - Code 1005
Director of Technical Services - Code 2000
NRL Historian - Code 2604
Dr. W. Ellis - Code 4000
Dr. J. Boris - Code 4040
Dr. M. Picone - Code 4040
Dr. M. Rosen - Code 4650
Dr. M. Haftel - Code 4665
Dr. S. Ossakow - Code 4700 (26 copies)
Dr. A. Ali - Code 4700.1
Dr. M. Friedman - Code 4700.1
Dr. R. Taylor - BRA (4700.1)
Dr. S. Gold - Code 4740
Dr. R. Meger - Code 4750
Dr. A. Robson - Code 4760
Dr. D. Murphy - Code 4763
Dr. R. Pechacek - Code 4763
Dr. G. Cooperstein - Code 4770
Dr. D. Colombant - Code 4790
Dr. R. Fernsler - Code 4790
Dr. I. Haber - Code 4790
Dr. R. F. Hubbard - Code 4790
Dr. G. Joyce - Code 4790 (25 copies)
Dr. Y. Lau - Code 4790
Dr. S. P. Slinker - Code 4790
Dr. P. Sprangle - Code 4790
B. Pitcher - Code 4790A
Code 4790 (20 copies)
Mr. P. Boris - SAIC (Code 4790)
Dr. J. Krall - SAIC (Code 4790) (25 copies)
Library - Code 2628 (2 copies)
D. Wilbanks - Code 2634
Code 1220

* Every name listed on distribution gets one copy except for those where extra copies are noted.

Air Force Office of Scientific Research
Physical and Geophysical Sciences
Bolling Air Force Base
Washington, DC 20332
Attn: Major Bruce Smith

Air Force Weapons Laboratory
Kirtland Air Force Base
Albuquerque, NM 87117
Attn: W. Baker (AFWL/NTYP)
D. Dietz (AFWL/NTYP)
Lt Col J. Head
R. W. Lemke

U. S. Army Ballistics Research Laboratory
Aberdeen Proving Ground, Maryland 21005
Attn: Dr. Donald Eccleshall (DRXBR-BM)
Dr. Anand Prakash
Dr. Clinton Hollandsworth

Avco Everett Research Laboratory
2385 Revere Beach Pkwy
Everett, Massachusetts 02149
Attn: Dr. R. Patrick
Dr. Dennis Reilly

Ballistic Missile Def. Ad. Tech. Ctr.
P.O. Box 1500
Huntsville, Alabama 35807
Attn: Dr. M. Hawie (BMDSATC-1)

Chief of Naval Material
Office of Naval Technology
MAT-0712, Room 503
800 North Quincy Street
Arlington, VA 22217
Attn: Dr. Eli Zimet

Commander
Space and Naval Warfare Systems Command
National Center 1, Room 8E08
Washington, DC 20363-5100
Attn: RADM Robert L. Topping

Cornell University
369 Upson Hall
Ithaca, NY 14853
Attn: Prof. David Hammer

DASIAC - DETIR
Kaman Tempo
25600 Huntington Avenue, Suite 500
Alexandria, VA 22303
Attn: Mr. F. Wimenitz

Defense Advanced Research Projects Agen
1400 Wilson Blvd.
Arlington, VA 22209
Attn: Dr. Shen Shey
Dr. H. L. Buchanan

Defense Nuclear Agency
Washington, DC 20305
Attn: Dr. I. Koch
Dr. Muhammad Owais (RAAE)

Department of Energy
Washington, DC 20545
Attn: Dr. Wilmot Hess (ER20:GTN,
High Energy and Nuclear Physics)
Mr. Gerald J. Peters (G-256)

Directed Technologies, Inc.
1500 Wilson Blvd. Suite 515
Arlington, VA 22209
Attn: Mr. Ira F. Kuhn
Dr. Nancy Chesser

C. S. Draper Laboratories
555 Technology Square
Cambridge, Massachusetts 02139
Attn: Dr. E. Olsson
Dr. L. Matson

General Dynamics Corporation
Pomana Division
1675 W. Mission Blvd.
P. O. Box 2507
Pomana, CA 92769-2507
Attn: Dr. Ken W. Hawko

Hy-Tech Research Corp.
P. O. Box 3422 FSS
Radford, VA 24143
Attn: Dr. Edward Yadlowsky

HQ Foreign Technology Division
Wright-Patterson AFB, OH 45433
Attn: TUTD/Dr. C. Joseph Butler

Institute for Defense Analyses
1801 N. Beauregard Street
Alexandria, VA 22311
Attn: Dr. Deborah Levin
Ms. M. Smith

Intelcom Rad Tech.
P.O. Box 81087
San Diego, California 92138
Attn: Dr. W. Selph

JAYCOR
11011 Torreyana Road
P. O. Box 85154
San Diego, CA 92138-9259
Attn: Dr. Franklin S. Felber
Dr. Seung Kai Wong

JAYCOR
39650 Libery Street, Suite 320
Freemont, CA 94538
Attn: Dr. Kendal Casey

Joint Institute for Laboratory
Astrophysics
National Bureau of Standards and
University of Colorado
Boulder, CO 80309
Attn: Dr. Arthur V. Phelps

Kaman Sciences
1500 Garden of the Gods Road
Colorado Springs, CO 80933
Attn: Dr. John P. Jackson

Kaman Sciences
P. O. Drawer QQ
Santa Barbara, CA 93102
Attn: Dr. W. Hobbs

La Jolla Institute
P. O. Box 1434
La Jolla, CA 92038
Attn: Dr. K. Brueckner

Lawrence Berkeley Laboratory
University of California
Berkeley, CA 94720
Attn: Dr. Edward P. Lee
Dr. Thomas Fessenden

Lawrence Livermore National Laboratory
University of California
Livermore, California 94550
Attn: Dr. Richard J. Briggs
Dr. Simon S. Yu
Dr. Frank Chambers
Dr. James W.-K. Mark, L-477
Dr. William Fawley
Dr. William Barletta
Dr. William Sharp
Dr. Daniel S. Prono
Dr. John K. Boyd
Dr. John Clark
Dr. George J. Caporaso
Dr. William E. Martin
Dr. Donald Prosnitz
Dr. A. C. Smith
Dr. John Stewart
Dr. Y. P. Chong
Major Kenneth Dreyer
Dr. Hans Kruger
Dr. Thaddeus J. Orzechowski
Dr. Michael R. Teague
Mr. John T. Weir

Dr. James E. Leiss
13013 Chestnut Oak Drive
Gaithersburg, MD 20878

Lockheed Missiles and Space Co.
3251 Hanover St.
Bldg. 205, Dept 92-20
Palo Alto, CA 94304
Attn: Dr. John Siambis

Los Alamos National Laboratory
P.O. Box 1663
Los Alamos, NM 87545
Attn: Dr. L. Thode
Dr. H. Dogliani, MS-5000
Mr. R. Carlson, MS-P940
Dr. Carl Ekdahl, MS-D410
Dr. Joseph Mack
Dr. Melvin I. Buchwald
Dr. David C. Moir

Maxwell Laboratories Inc.
8888 Balboa Avenue
San Diego, CA 92123
Attn: Dr. Ken Whitham

McDonnell Douglas Research Laboratories
Dept. 223, Bldg. 33, Level 45
Box 516
St. Louis, MO 63166
Attn: Dr. Evan Rose
Dr. Carl Leader
Dr. Frank Bieniosek
Dr. John Honig

Mission Research Corporation
1720 Randolph Road, S.E.
Albuquerque, NM 87106
Attn: Dr. Brendan Godfrey
Dr. Thomas Hughes
Dr. Lawrence Wright
Dr. Kenneth Struve
Dr. Michael Mostrom
Dr. Dale Welch

Mission Research Corporation
P. O. Drawer 719
Santa Barbara, California 93102
Attn: Dr. C. Longmire
Dr. N. Carron

National Bureau of Standards
Gaithersburg, Maryland 20760
Attn: Dr. Mark Wilson

Naval Postgraduate School
Physics Department (Code 61)
Monterey, CA 93940
Attn: Prof. John R. Neighbours
Prof. Fred Buskirk
Prof. Kai Woehler
Prof. Xavier Maruyama

Naval Surface Warfare Center
White Oak Laboratory
Code R-41
Silver Spring, Maryland 20903-5000
Attn: Dr. B. Hui
Mr. W. M. Hinckley
Dr. M. H. Cha
Dr. H. S. Uhm
Dr. R. Fiorito
Dr. K. T. Nguyen
Dr. R. Stark
Dr. H. C. Chen
Dr. D. Rule
Dr. Matt Brown
Mrs. Carolyn Fisher (G42)
Dr. Eugene E. Nolting (H23)

Office of Naval Research
800 North Quincy Street
Arlington, VA 22217
Attn: Dr. C. W. Roberson
Dr. F. Saalfeld

Office of Naval Research (2 copies)
Department of the Navy
Code 01231C
Arlington, VA 22217

Office of Under Secretary of Defense
Research and Engineering
Room 3E1034
The Pentagon
Washington, DC 20301
Attn: Dr. John MacCallum

ORI, Inc.
1375 Piccard Drive
Rockville, MD 20850
Attn: Dr. C. M. Huddleston

Physics International, Inc.
2700 Merced Street
San Leandro, CA. 94577
Attn: Dr. E. Goldman
Dr. James Benford
Dr. George B. Frazier
Mr. Ralph Genuario

Princeton University
Plasma Physics Laboratory
Princeton, NJ 08540
Attn: Dr. Francis Perkins, Jr.

Pulse Sciences, Inc.
600 McCormack Street
San Leandro, CA 94577
Attn: Dr. Sidney Putnam

Pulse Sciences, Inc.
2001 Wilshire Boulevard
Suite 600
Santa Monica, CA 90403
Attn: Dr. John R. Bayless
Dr. R. Adler

The Rand Corporation
2100 M Street, NW
Washington, DC 20037
Attn: Dr. Nikita Wells
Mr. Simon Kassel

Sandia National Laboratory
Albuquerque, NM 87115
Attn: Dr. David Hasti/1272
Dr. Collins Clark
Dr. John Freeman/1241
Dr. Charles Frost
Dr. George Kamin/1274
Dr. Gordon T. Leifeste
Dr. Gerald N. Hays
Dr. James Chang
Dr. Michael G. Mazarakis/1272
Dr. John Wagner/1241
Dr. Ron Lipinski/1274
Dr. James Poukey
Dr. Milton J. Clauser/1261
Dr. Kenneth R. Prestwich/1240
Dr. Kevin O'Brien
Dr. Isaac R. Shokair
Dr. J. Pace VanDevender/1200

Science Applications Intl. Corp.
P. O. Box 2351
La Jolla, CA 92038
Attn: Dr. Rang Tsang

Science Applications Intl. Corp.
5150 El Camino Road
Los Altos, CA 94022
Attn: Dr. R. R. Johnston
Dr. Leon Feinstein
Dr. Douglas Keeley
Dr. E. Roland Parkinson
Dr. Charles Yee

Science Applications Intl. Corp.
1710 Goodridge Drive
McLean, VA 22102
Attn: Mr. W. Chadsey
Dr. A Drobot
Dr. K. Papadopoulos
Dr. William W. Rienstra
Dr. Alan J. Toepfer
Dr. Alfred Mondelli
Dr. D. Chernin

Science Research Laboratory, Inc.
1600 Wilson Boulevard
Suite 1200
Arlington, VA 22209
Attn: Dr. Joseph Mangano
Dr. Daniel Birx

DIRECTOR OF RESEARCH
U.S. NAVAL ACADEMY
ANNAPOLIS, MD 21402
2 COPIES

Commander
Space & Naval Warfare Systems Command
PMW-145
Washington, DC 20363-5100
Attn: CAPT J. D. Fontana
LT Fritchie

SRI International
PSO-15
Molecular Physics Laboratory
333 Ravenswood Avenue
Menlo Park, CA 94025
Attn: Dr. Donald Eckstrom
Dr. Kenneth R. Stalder

Strategic Defense Initiative Org.
1717 H Street, N. W.
Washington, DC 20009
Attn: Lt Col R. L. Gullickson
Dr. D. Duston

Strategic Defense Initiative Office
Directed Energy Weapons Office, The Pentagon
Office of the Secretary of Defense
Washington, DC 20301-7100
Attn: Dr. C. F. Sharn (OP0987B)

Titan/Spectron, Inc.
P. O. Box 4399
Albuquerque, NM 87196
Attn: Dr. R. Bruce Miller
Dr. John Smith

Titan Systems, Inc.
2685 Marine Way
Suite 1408
Mountain View, CA 94043
Attn: Dr. Kenneth W. Billman

Titan Systems, Inc.
9191 Towne Centre Dr.-Suite 500
San Diego, CA 92122
Attn: Dr. R. M. Dowe

University of California
Physics Department
Irvine, CA 92664
Attn: Dr. Gregory Benford
Dr. Norman Rostoker

University of California
San Diego, CA 92110
Attn: Dr. Marshall N. Rosenbluth